Inorganic Chemistry

pubs.acs.org/IC

Article

# Fluxionality Modulating the Magnetic Anisotropy in Lanthanoarene [($\eta C_nR_n$)$_2$Ln(II/III)] ($n$ = 4−8) Single-Ion Magnets

Abinash Swain,[†] Rupesh Kumar Tiwari,[†] Munmun Khatua, and Gopalan Rajaraman*

Cite This: *Inorg. Chem.* 2023, 62, 9552−9562

Read Online

ACCESS | Metrics & More | Article Recommendations | Supporting Information

**ABSTRACT:** Lanthanoarenes have emerged as the best bet for the futuristic application of single-ion magnets in information storage devices. While dysprosocenium molecules with various substituents at the arene ring exhibit a very large blocking temperature, the corresponding Er(III) analogues do not, and this is reversed if the size of the arene ring is eight. Using a combination of ab initio CASSCF and DFT-based molecular dynamics (MD) study, we have explored 25 Dy(III)/Er(III)/Ho(II)/Tb(II)/Dy(II) arene complexes with the ring size varying from 4 to 8 to understand the differences observed and decipher the correlation of structure to the spin dynamics behavior. Among the oxidation state of +2 complexes studied, Tb(II) exhibits the highest barrier, with the Cp−Tb−Cp angle being linear. Further, one of the four-membered arene model studied exhibits a very large barrier of 1442 cm$^{-1}$, suggesting a potential high-blocking SIM. While bulky substituents at the arene ring help increase the axiality and the $C_R$−Ln−$C_R$ angle, this also fetches several agostic C−H···Ln interactions, which injects transverse anisotropy. Furthermore, MD coupled with the CASSCF study reveals that the fluxional behavior of the arene ring generates several rotational conformers that are even accessible at lower temperatures offering a shortcut to the magnetization relaxation process. The importance of structural fluctuations in controlling the magnetic anisotropy by choosing apt metal-ion/ring partners and the corresponding substituents has been highlighted to offer clues to the futuristic SIM design.

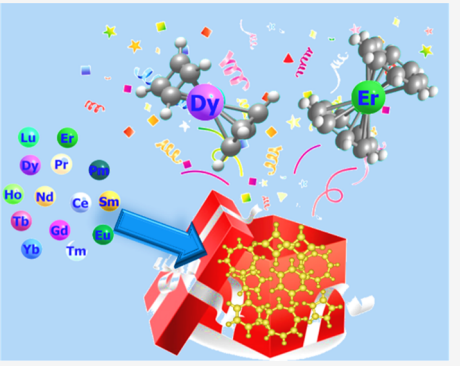




## INTRODUCTION

Single-ion magnets (SIMs)[1] based on Dy(III) ions are gaining attention in recent years as molecules based on dysprosocenium exhibit very high blocking temperatures,[2] rekindling a ray of hope for potential applications such as high-dense information storage devices.[3,4] Among many types of lanthanide molecules reported, organometallic lanthanide complexes gain significant attraction as they often yield very large barrier height for magnetization reversal ($U_{eff}$) and high blocking temperatures ($T_B$).[5−7] Among these, cycloarene ligands are attractive as they generally impose very high symmetry around the metal ion, which helps to suppress the quantum tunneling of magnetization (QTM)[8,9] and offer larger crystal field splitting of $m_J$ levels—thanks to strongly delocalized $\pi$-electron clouds that readily mix with the frontier orbitals of Lanthanide (III) ions.[10] Particularly, when the charge distribution around the Ln$^{III}$ ion exhibits $C_n$ ($n \geq 7$), $C_{5h}/D_{5h}$ (for which the symmetry axis is fivefold, i.e., $C_5$), $S_8/D_{4d}$, and $S_{12}/D_{6d}$ point group, the QTM is found to be quenched, and many of these points groups are accessible for cycloarene ligands.[11,12] The cycloarene ligands are not only suitable for Dy(III) ion with an oblate electron density but also for Er(III) ion with prolate electron density (if $m_J = \pm 15/2$ is stabilized as the ground state) if the ring size is much larger.[13] For example, among the Er(III) SIMs, the [Er(COT)$_2$]$^-$ (COT = cyclooctatriene) has one of the highest blocking temperatures reported (11 K, 35 Oe/s sweep rate).[14,15] Thus, the marriage of a suitable metal ion with an appropriate cycloarene is of utmost importance for attaining large blocking temperatures. Second, these molecules are known to exhibit fluxional behavior whose role in controlling $T_B$ is hitherto unknown.[16] In this work, employing an array of theoretical tools such as CASSCF/RASSI-SO/SINGLE_ANISO,[17] DFT (B3LYP/TZVP),[18] and molecular dynamics (MD; PBE/DZVP-SR-GTH) , we attempt to untangle these puzzles and offer clues to enhance blocking temperatures further. The role of theoretical calculations based on ab initio CASSCF methods in the design of SIMs is well established[19] and is even successful in predicting new lines of molecules such as Ln$_2$@C$_{79}$N.[20,21]

Here, we have studied the mechanism of magnetic relaxation in Dy/Er(III)/Ln(II) cycloarene complexes with ring sizes varying from four to eight. MD followed by CASSCF calculations were performed to understand the role of

Received: March 23, 2023
Published: June 6, 2023

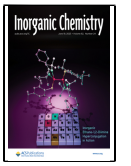




https://doi.org/10.1021/acs.inorgchem.3c00956
*Inorg. Chem.* 2023, 62, 9552−9562

fluxionality/stability in determining the barrier height ($U_{cal}$) that is directly correlated to $T_B$ values as they influence the crystal field (CF) parameters.[22] This further allows us to analyze the effect of structural vibrations on the crystal field over different time intervals as there is an exchange of energy taking place between the molecule and thermal bath via vibrations over the time intervals. Using classical MD coupled with ligand field theory (LFT) analysis, calculations performed on $Tb^{3+}$ ion containing metallopeptidase reveal that local vibrations are key to understanding the spin dynamics in lanthanide complexes and affirm the importance of performing molecular dynamics calculations to understand the spin dynamics.[23−27] Further, another study suggests that in SIMs, only the low-energy region of the phonon spectrum is expected to participate in the relaxation process. Motivated by this work, here, we have looked into the variation of crystal field parameters at different temperatures for lanthanoarene complexes.

We have considered 25 complexes $[(\eta^p\text{-}C_nR_n)_2Ln]^m$ [$m$ = −3, −1, +1, +3; $n$ = 4−8; $p$ = 2−8; R = H, Ln = Dy(**$^{nH}$Dy**), Er(**$^{nH}$Er**); R = H−Me Ln = Dy(**$^{nHMe}$Dy**), Er(**$^{nHMe}$Er**); R = Me, $SiMe_3$ Ln = Dy(**$^{nMeSi}$Dy**), R = $SiMe_3$, Dy(**$^{nSi}$Dy**)] of Dy(III) and Er(III)/Ln(II) complexes with various cycloarene ligations (see Figures 1 and S1). Most of the studied structures are

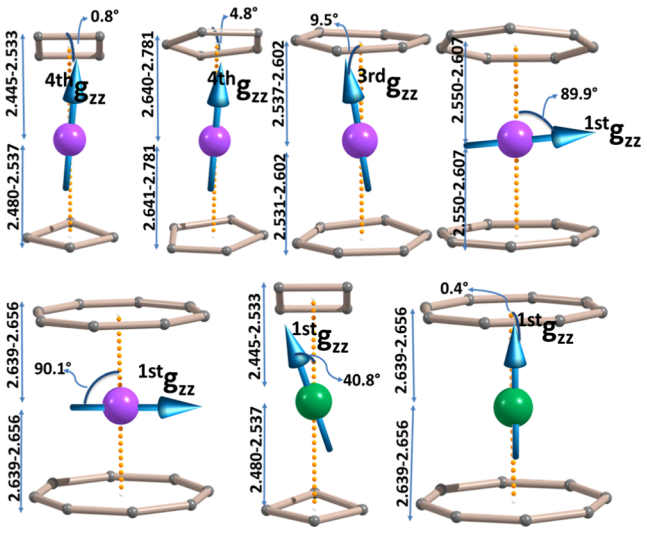


**Figure 1.** DFT optimized model structures for complexes **$^{4H}$Dy**, **$^{5H}$Dy**, **$^{6H}$Dy**, **$^{7H}$Dy**, **$^{8H}$Dy**, **$^{4H}$Er**, and **$^{8H}$Er** along with their main magnetic axis (orange dotted line) for the ground state and the anisotropic axis for the excited state (blue arrow) causing magnetic relaxation. Color code, violet = Dy, green = Er, gray = C, H atoms are omitted for clarity.

known with alkyl/aryl substituents, and magnetic characterizations were reported for some of them.[2,6,28−30] All the structures were modelled and optimized using DFT and G09 suite[31] except for **$^{8H}$Dy** and **$^{8H}$Er**, where X-ray geometries were utilized as such. The geometry and selected structural parameters for all 25 models are given in Supporting Information (Figure S1 and Table S2). Here, we aim to answer the following open questions: (i) What is the role of the fluxional behavior of the arene ligand in determining the blocking barrier/temperatures? (ii) Can the size of the arene ring be utilized to alter the nature of Ln-ligand interaction viz−a−viz axial vs equatorial? (iii) How important are the agostic interactions in dictating the blocking barriers in this class of molecules? (iv) Can DFT-based molecular dynamics be used to probe the spin dynamics of such systems? (v) How the magnetization relaxation alters when the metal center is reduced from Ln(III) to Ln(II)?

## COMPUTATIONAL DETAILS

**DFT and MD Calculations.** For static DFT geometry optimizations, G09 suite of programs was employed.[18,32] Here, we have used a UB3LYP[18] functional and Jorge-TZP[33,34] basis set for lanthanide and 6-31G*[35] for the rest of the atoms (both for $Ln^{3+}$ and $Ln^{2+}$ systems).[36,37] These basis sets are found to reproduce atomic charges and geometry accurately compared to many effective core potential or SARC basis sets.[34] Further, the geometry computed for the **$^{5HMe}$Dy** using this setup yields structural parameters that match the analogues X-ray geometry, offering confidence in the methodology employed (see Table S3). Additionally, we have performed the AIM (atoms in molecules) analysis with the AIM2000 programme package to determine the coordination number of $Ln^{3+}$ ions to gain clues into the nature of bonding.[38]

The DFT-based molecular dynamics simulations have been carried out using the Cp2K 6.1[39] program on model systems employing the *NVT* module on the gas phase with the cell containing a single molecule.[40] To perform MD, Ln(III) ion was replaced by Y(III) ion and a DZVP-MOLOPT-SR-GTH basis set for Y(III), and for the rest of the atom, a DZVP-MOLOPT-GTH level of basis set has been employed. These calculations were performed using unrestricted PBE functional, which has a proven track record of yielding good geometries at an affordable computational cost.[41] A velocity scaling thermostat has been applied throughout the simulation to maintain the temperature at 300 K. The trajectory up to 2000 fs has been generated for all the complexes. Further frequency calculations were also performed on the snapshots generated from the trajectories using G09 (methodology same as above) to understand how they vary with respect to the equilibrium vibrations (see Tables S11−13). Note that the frequencies given at the lower energy levels are likely to play an important role in the spin relaxation mechanism, as evidenced in the earlier work.[22,42]

**Ab Initio CASSCF Calculations.** All ab initio CASSCF calculations have been performed using the MOLCAS 8.01 package.[43−46] All CASSCF calculations have been employed with an active space of nine and eleven active electrons in seven 4f orbitals of Dy(III) and Er(III), respectively. All the electronic states arising from the active spaces were optimized self consistently for the orbitals and coefficients of the individual configurations. The DKH Hamiltonian has been used to take into account the relativistic effects. Having these active spaces, we have allowed 21 sextet roots for Dy(III) and 35 quartet and 112 doublet roots for Er(III) in CI (spin−orbit interactions described within AMFI approximation) procedure. Further, to speed up the calculations, Cholesky decomposition was used with the default cut-off values. For the smallest system, **$^{4H}$Dy** 130 doublets, 128 quartets, and 21 sextets have been taken for Dy, which yields results that are very similar to that of considering only 21 sextet states. Therefore, for higher member rings, only 21 sextet states were taken into account. Mixing of these states was performed using the RASSI-SO[43−46] module for computing spin−orbit states. These spin−orbit states were then used to calculate the g-tensors, crystal field splitting, magnetic blocking diagram, and other magnetic properties using the SINGLE_ANISO module.[17] Both Dy(III)


https://doi.org/10.1021/acs.inorgchem.3c00956
Inorg. Chem. 2023, 62, 9552−9562

Table 1. Ab Initio Computed $U_{cal}$ Values For All 25 Complexes Computed Along With Their Ground $g_{zz}$ Value and the $C_R$−Ln−$C_R$ Angles[a]

| model complexes | $U_{cal}/U_{eff}$ ($cm^{-1}$) | $g_{xx}/g_{yy}/g_{zz}$ | angles (°) |
|---|---|---|---|
| $[Dy\{\eta^3\text{-}C_4(SiMe_3)_4H\}\{\eta^4\text{-}C_4(Si\ Me_3)_3\text{-}k\text{-}(CH_2SiMe_2)Na]^{\infty}$ | 309 | | 159.26 |
| $^{4H}Dy$ | 961.2, 3rd | 0.0/0.0/19.997 | 146.9 |
| $^{4H}Er$ | 15.7, 0th | 7.259/6.918/3.579 | 146.9 |
| $^{4HMe}Dy$ | 642.9, 2nd | 0.0/0.0/19.956 | 136.2 |
| $^{4HMe}Er$ | 52.6, 0th | 0.019/1.093/14.747 | 136.2 |
| $^{4MeSi}Dy$ | 1255.9, 4th | 0.0/0.0/19.976 | 152.3 |
| $^{4Si}Dy$ | 1442.0, 5th | 0.0/0.0/19.999 | 157.4 |
| $[Dy(Cpttt)_2]^+$ | 1223, 6th | | 152.6[2,50] |
| $^{5H}Dy$ | 912.3, 4th | 0.0/0.0/20.0079 | 134.5 |
| $^{5H}Er$ | 36.0, 0th | 0.531/1.764/14.892 | 134.5 |
| $^{5HMe}Dy$ | 1102.7, 5th | 0.0/0.0/20.013 | 147.6 |
| $^{5HMe}Er$ | 17.8, 0th | 0.205/0.817/15.082 | 147.6 |
| $[Tb(Cp^{iprS})_2)]$ | 1205 | | 180[51] |
| $^{5Me}Dy(II)$ | 1259.8, 2nd | 0.0/0.0/22.009 | 179.1 |
| $^{5Me}Tb(II)$ | 2039, 5th | 0.0/0.0/20.015 | 179.1 |
| $^{5Me}Ho(II)$ | 773, 3rd | 0.0/0.0/22.007 | 179.1 |
| $[(\eta^6\text{corannulene})Dy(C_6H_6)]$ | 608, 4th | 0.0/0.0/19.960 | 156.5[52] |
| $^{6H}Dy$ | 671.8, 3rd | 0.0/0.0/20.005 | 174.6 |
| $^{6H}Er$ | 61.9, 0th | 1.864/1.248/8.327 | 174.6 |
| $^{6HMe}Dy$ | 528.3, 3rd | 0.0/0.0/20.004 | 172.6 |
| $^{6HMe}Er$ | 49.3, 0th | 1.108/1.257/8.372 | 172.6 |
| $[KEr_2(\eta^7\text{-}C_7H_7)(N(SiMe_3)_2)_4]$ | 40 | | -[53] |
| $^{7H}Dy$ | 20.4, 1st | 0.024/0.089/11.935 | 163.2 |
| $^{7H}Er$ | 251.3, 1st | 0.0/0.0/17.948 | 163.2 |
| $^{7HMe}Dy$ | 22.7, 1st | 0.063/0.218/12.331 | 164.2 |
| $^{7HMe}Er$ | 253.6, 1st | 0.0/0.0/17.932 | 164.2 |
| $Dy[(COT)_2]^-$ | 9 | | 180[17] |
| $Er[(COT)_2]^-$ | 150 | | 180[15] |
| $^{8H}Dy$ | 70, 2nd | 0.004/0.008/16.684 | 173.8 |
| $^{8H}Er$ | 144.2, 2nd | 0.0/0.0/17.864 | 173.8 |
| $^{8HMe}Dy$ | 37.6, 2nd | 0.075/0.084/12.016 | 180.0 |
| $^{8HMe}Er$ | 255.7, 2nd | 0.0/0.0/17.944 | 180.0 |

[a]Here $C_R$ refers to the center of the ring. The excited state via the magnetic relaxation predicted is given along with the $U_{eff}$ values.

and Er(III) have eight low-lying Kramers doublet (KD) for which the g-tensor has been calculated. The low-lying states that arise due to $m_J = \pm 15/2$ multiplet on individual Ln(III) sites are provided in Tables S4,S5,S7. For the Ln(III) ion, an ANO-RCC-TZVP level of basis set, and for the rest of the atoms, an ANO-RCC-DZV level of basis set from the ANO-RCC library has been utilized.[47−49] For the complex $^{4H}$**Dy**, benchmarking has been done by considering a higher basis set for C and H atoms from ANO-RCC-DZV to ANO-RCC-TZV to ANO-RCC-TZVP, which enhances the energy barrier ($U_{cal}$) from 961 to 1009 and 1020.6 $cm^{-1}$, respectively, with 4th excited state relaxation; the angle between the ground state anisotropy axis and excited anisotropic axis reduces by improving the basis set, and the results were compared in the Table S4. Although a better basis set improves the results, the changes are only marginal. Similar to Ln(III), for Ln(II) complexes, an ANO-RCC-TZVP level of basis set for the Ln(II) ion and ANO-RCC-DZV basis set for other atoms have been used to perform CASSCF/RASSI-SO/SINGLE_ANISO calculations. Extended active space of CAS-(9,8), CAS-(10,8), and CAS-(11,8) have been used for $Tb^{II}(4f^8 5d^1 6s^0/4f^8 5d^0 6s^1)$, $Dy^{II}(4f^9 5d^1 6s^0/4f^9 5d^0 6s^1)$, and $Ho^{II}(4f^{10} 5d^1 6s^0/4f^{10} 5d^0 6s^1)$ complexes, respectively. Here, we have taken either one $5d_z^2$ or one 6s orbital in our orbital space, as suggested earlier.[51] Our earlier studies on strongly covalent systems such as actinide, which are analogues to Ln(II) in terms of metal−ligand covalency, also recommend the inclusion of $5d_z^2$ orbital in the reference space.[54] For these calculations, we have computed 8 octets and 21 sextets for Tb(II), 7 septets and 140 quintets for Dy(II), and 21 sextets and 128 quartets for Ho(II) roots, respectively. There are three $Ln^{II}(Cp^{Me5})_2$ ($^{5Me}$Ln(II); Ln = Tb, Dy and Ho) complexes that have been considered here. These complexes were modelled by replacing the iPr5 (iso-propyl) group with the $-CH_3$ group of $Ln(Cp^{iprS})_2$, which has been synthesized by Long and co-workers.[51]

The following Hamiltonian has been used for calculating the crystal field parameters:

$$H_{CF} = \sum_{k,q} B_k^q O_k^q$$

where, $O_k^q$ = extended Stevens operator, $k$ = rank of ITO = 2, 4, 6, and $q$ = component of the ITO = $-k, -k+1, ..., 0, ..., k$. The $B_2^0$ and $B_4^0$ for both the Dy and Er center are of negative value, indicating axial contribution.[55,56] We have used the following common formula to denote 25 geometries $[(\eta^p\text{-}C_nR_n)_2Ln]^m$. Here, $\eta^p$ represents the hapticity obtained using AIM calculations (see below) with the p-indicating the number of


https://doi.org/10.1021/acs.inorgchem.3c00956
Inorg. Chem. 2023, 62, 9552−9562

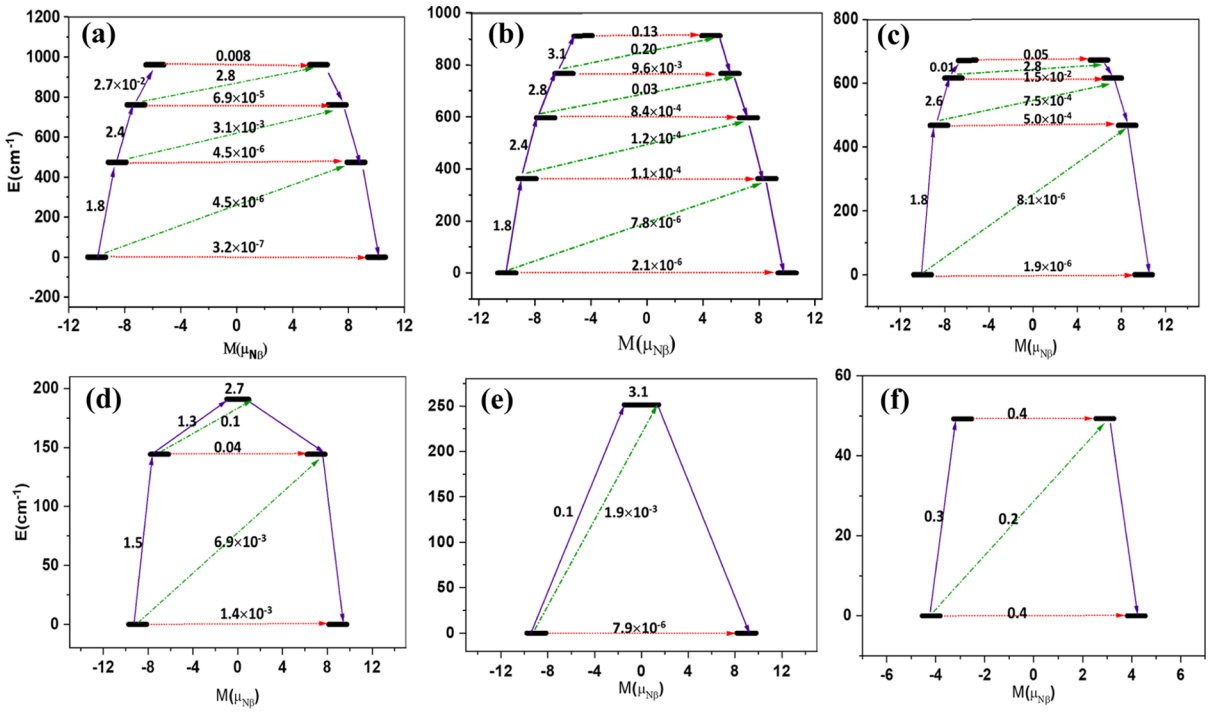


**Figure 2.** Energy of the lowest-lying Kramers doublet with relaxation dynamics for complexes $^{4H}$**Dy** (a), $^{5H}$**Dy** (b), $^{6H}$**Dy** (c), $^{8H}$**Er** (d), $^{7H}$**Er** (e), and $^{6H}$**Er** (f). The red dotted line represents the QTM processes, the solid blue arrow represents the direct TA-QTM, and the green line corresponds to the Raman/Orbach processes. Numbers on the arrows indicate the transition probabilities between the corresponding states.

bonds. The $C_nR_n$ indicates the size of the arene ring where $n$ = 4−8, and R = H, Me, $SiMe_3$. Thus, $^{4H}$**Dy** represents $[(C_4H_4)_2Dy]^-$, $^{4MeSi}$**Dy** represents $[(C_4(Me)_2(SiMe_3)_2)_2Dy]^-$, and $^{4Si}$**Dy** represents $[(C_4(SiMe_3)_4)_2Dy]^-$. A full table of abbreviations for each complex is given in Supporting Information (Table S1).

## RESULTS AND DISCUSSION

**Structure and Bonding of Lanthanoarenes(III).** For all the $[(\eta^p\text{-}C_nR_n)_2Ln]^m$ complexes studied, the Ln−C distance was found to be the shortest for $^{4H}$**Dy**/**Er** $[(\eta^2{-}\eta^3\text{-}C_4R_4)_2Dy]^-$ (2.445 Å) and longest for $^{5H}$**Dy**/**Er** $[(\eta^p\text{-}C_5R_5)_2Ln]^+$ ($p$ = 2 or 3; 2.781 Å) complexes. The $C_R$−Ln−$C_R$ ($C_R$ represents the center of the ring) angle was estimated to be 146.9, 147.6, 174.6, 163.2, and 173.9° for $n$ = 4, 5, 6, 7, and 8, respectively (see Figure 1 and Table S2). The Ln−X (X = center of the arene ring) bond length increased as we moved from 4 to 6 but then dropped substantially for seven and even more for eight-membered rings (see Tables 1 and S2). The geometrical parameters computed are in agreement with the available X-ray structures. For the five-membered ring sandwich complex, $^{5HMe}$**Dy**, the structural parameters along with the low-lying energy splitting for the eight Kramers doublet has been compared with the experimentally reported X-ray ($[Dy(Cp^{ttt})_2]^+$) complex (Supporting Information Table S3). Selected structural parameters of the X-ray and the optimized geometries reveal only a slight variation in the structural parameters with Ln−C distance of 2.412 Å vs 2.322 Å and $C_R$−Ln−$C_R$ angle of 147.6° vs 152.5° (∼3% deviation in structural parameters). Further, ab initio calculations performed on these two geometries reveal minor variation in the magnetic anisotropy and effective energy barrier ($U_{eff}$ estimated to be 1102 $cm^{-1}$ vs 1168 $cm^{-1}$, i.e., ∼5% deviation is noted), offering confidence in the geometries as well the magnetic characteristics of the model employed to the X-ray geometries.

To understand the Ln−C bonding, AIM calculations were performed (see Computational Details), which reveals that the ligand hapticity is not always the same as the number of ring carbon atoms (the computed hapticity based on AIM analysis is given in Table S2). This analysis further indicates that there is a variation in the Ln−C distances with unsymmetrical Ln−C bonding in smaller arene ring complexes. For example, in $^{4H}$**Dy**, the hapticity is found to be $\eta^2$ with one ring and $\eta^3$ with another. Substituting H-atom in $^{4H}$**Dy** by $SiMe_3$ or by two Me/$SiMe_3$ leads to increased hapticity with $\eta^3$−Ln−$\eta^4$ bonding observed in $^{4Si}$**Dy**. The expected $\eta^4$−Ln−$\eta^4$ bonding is seen in $^{4MeSi}$**Dy**. The bonding and the geometry predicted here for the $^{4MeSi}$**Dy** agree with the analogues X-ray structure reported, offering confidence in the methodology chosen. A similar trend is noticeable for the five- and six-membered rings studied, where enhancing the bulkiness enhances the hapticity (Table S2). However, the trend is reversed for seven- and eight-membered rings, with $\eta^7$−Ln−$\eta^7$ noticed for $^{7H}$**Dy**. Summing the computed Laplacian for Ln−C bond predicts the following order in four-membered ring complexes $^{4H}$**Dy** < $^{4HMe}$**Dy** < $^{4MeSi}$**Dy** < $^{4Si}$**Dy**, and this predicted bond strength is correlated directly to the CF splitting of the 4f-orbitals and the anisotropy. Quite interestingly, a similar trend is also noticeable for five- and six-membered rings, with enhancing the bulkiness of the substituents enhancing the Ln−C bond strength. This order was also found to be reversed for seven- and eight-membered ring systems.

Further, our calculations reveal strong Ln···H−C agostic interactions in $^{4HMe}$**Dy**, $^{4Si}$**Dy**, $^{5H}$**Dy**, and $^{5HMe}$**Dy** geometries with the shortest Ln···H distance of 2.322, 2.708, 3.157, and 3.584 Å, respectively. The closest Ln···H distance is observed in $^{4HMe}$**Dy** (the bond critical point $\nabla^2\rho$ is −0.027), and the


https://doi.org/10.1021/acs.inorgchem.3c00956
Inorg. Chem. 2023, 62, 9552−9562

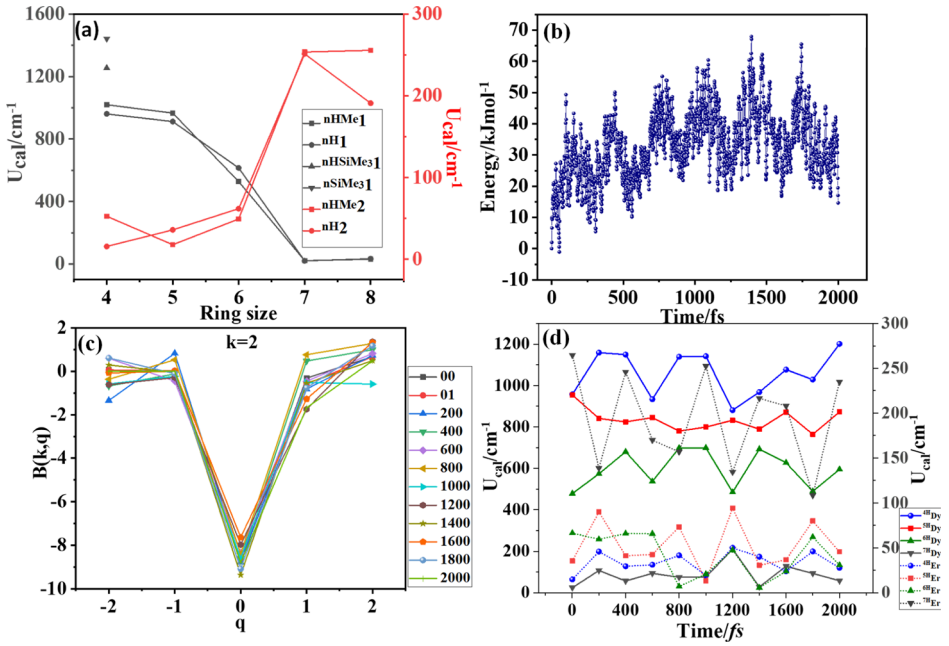


**Figure 3.** (a) Variation of $U_{cal}$ for different ring sizes for both Dy(III) and Er(III) for all the model complexes. (b) Profile of MD obtained for different structures of $^{4H}$**Dy** at a different time up to 2000 fs with the energy margin of 80 kJ mol$^{-1}$. (c) Variation of crystal field parameter $B(k,q)$ vs $q$ at $k$ = 2 for the different structures at different scans for $^{4H}$**Dy**. (d) $U_{cal}$ value was obtained for different ring sizes for Dy(III) and Er(III) complexes at 200 fs intervals.

moderate interaction is in the $^{4Si}$**Dy** ($\nabla^2\rho$ = −0.010; 2.687 Å). For the latter two, the interaction is almost negligible. These agostic interactions are likely to offer a significant transverse ligand field and, therefore, critical to magnetization relaxation and QTM for smaller ring systems (vide infra).

**Ab Initio Estimation of Barrier Heights for the Magnetization Reversal.** For all 25 geometries, ab initio CASSCF calculations were performed (see Computational Details), and the magnetization blockade barrier was developed to estimate the barrier height ($U_{cal}$, see Table 1).[57,58]

**Biscyclobutadienyl Lanthanide Complexes.** Among all the Dy(III) sandwich complexes we have studied, the four-membered $^{4MeSi}$**Dy** $[(\eta^4\text{-}C_4H_2(SiMe_3)_2)_2Dy]^-$ and $^{4Si}$**Dy** $[(\eta^4\text{–}\eta^3\text{-}C_4(SiMe_3)_4)_2Dy]^-$ emerged as the best SIM showing an $U_{cal}$ value of 1256 and 1442 cm$^{-1}$ (Table 1) relaxing via 4th and 5th excited states, respectively (Figure S10). The $[(\eta^2\text{–}\eta^3\text{-}C_4H_4)_2Dy]^-$ shows a $U_{cal}$ value of 961.2 cm$^{-1}$, as it relaxes via the 3rd excited level (Figure 2a). Comparing these three complexes, we have found that the bulkier substitution on the arene ring increases the $U_{cal}$ values. The strong electron donor capability of the substituents such as $SiMe_3$ enhances the strength of Ln-arene bonding, leading to shorter Dy−C bonds (Table S2). For $[(\eta^3\text{–}\eta^3\text{-}C_4H_2Me_2)_2Dy]^-$ molecule, the $U_{cal}$ value is estimated to be 643 cm$^{-1}$ (Figure S10), which is substantially smaller compared to other geometries, and this is due to significant C−Dy−C bending observed in this structure (Table S2). Moreover, the H atom of the methyl substituent at the arene ring was found to interact strongly with Dy(III) ion via agostic interaction. This agostic interaction provides a significant transverse field and causes QTM to occur at a lower excited state causing faster relaxation. Computed CF parameter $B_2^0$ is large and negative and follows the $^{4Si}$**Dy** > $^{4MeSi}$**Dy** > $^{4H}$**Dy** > $^{4HMe}$**Dy** order, same as the computed $U_{cal}$ values (Figures 3a, S2−S4, Table S2) for these complexes. A molecule similar to this predicted geometry has been reported by Layfield and co-workers ($[Dy\{\eta^3\text{-}C_4(SiMe_3)_4H\}\{\eta^4\text{-}C_4(SiMe_3)_3\text{-}\kappa\text{-}(CH_2SiMe_2\}Na]^\infty$) with a relatively smaller $U_{eff}$ value (309 cm$^{-1}$) due to Ln···H interactions.[6] The same complex with Er(III) ion, on the other hand, (complex $^{4H}$**Er**) exhibits no SIM characteristics as all complexes have significant mixing of excited states with the ground state leading to a very strong QTM (Figure S11). Because of the prolate nature of the ground state $m_J$ level, the computed $g_{zz}$ axis is tilted by 89.9° from the pseudo-$C_4$ axis (Figure 1). Among these complexes, as the bulkiness of the substituents in the carbon increases, the CF splitting increases and QTM probability decreases, and this is due to a weaker equatorial ligand field offered by these substituents via non-covalent interactions (Figures S2−S4).

**Biscyclopentadienyl Lanthanide Complexes.** Four molecules were modelled in this class of compounds. The mechanism of the magnetization relaxation developed for $^{5H}$**Dy**/**Er** and $^{5HMe}$**Dy**/**Er** is shown in Figures 2b and S12,S13. Our calculations yield an $U_{cal}$ value of 912 and 1103 cm$^{-1}$ for the $^{5H}$**Dy** and $^{5HMe}$**Dy** complexes, respectively, with the relaxation found to occur via 4th and 5th excited states, respectively (Figures 2b and S12). These findings are broadly in agreement with earlier studies on similar complexes.[2,19,24] For the $^{5H}$**Er** and $^{5HMe}$**Er** complexes, a strong QTM is found at the ground state with little to no barrier, as significant transverse anisotropy is computed ($g_{xx}$ = 0.5315, $g_{yy}$ = 1.7647 and $g_{zz}$ = 14.8928 and $g_{xx}$ = 0.2051, $g_{yy}$ = 0.8170 and $g_{zz}$ = 15.0822) for $^{5H}$**Er** and $^{5HMe}$**Er** (Table S10), respectively, (see Figure S12). The $g_{zz}$ axis is found to be tilted by ∼68.7° from the pseudo-$C_5$ axis. Both the direction of the anisotropy and strong transverse components computed agree with earlier theoretical studies and EPR spectroscopic data.[59]

**Biscyclohexatrienyl Lanthanide Complexes.** The mechanism of magnetization relaxation developed for four models in this class is shown in Figure 2c,f (also Figures S14


https://doi.org/10.1021/acs.inorgchem.3c00956
Inorg. Chem. 2023, 62, 9552−9562

and S15). Although zero valent Dy/Er complexes with such arene complexes were reported in the 90s, their magnetic properties by sandwiching a trivalent Lanthanide ion have not been explored yet.[60−62] The $U_{cal}$ value estimated for $^{6H}$**Dy** is 671.8 cm$^{-1}$ exhibiting still a strong axiality ($g_{xx}$ = 0.0, $g_{yy}$ = 0.0 and $g_{zz}$ = 20.0052) with the methyl substitution $^{6HMe}$**Dy** found to diminish the $U_{cal}$ value to 528 cm$^{-1}$. Increasing the arene ring props up the axiality in Er complexes; however, the transverse anisotropy is still stronger, leading to ground state QTM with small barriers (62.0 and 49.3 cm$^{-1}$ for $^{6H}$**Er** and $^{6HMe}$**Er** complexes, respectively). For the Er analogue, the $g_{zz}$ axis is found to be tilted by ∼77° with respect to the pseudo-$C_6$ axis, suggesting improvement in anisotropy upon expansion of the arene ring.

**Biscycloheptatrienyl/Octatetrienyl Lanthanide Complexes.** For seven-membered systems, $^{7H}$**Dy**, $^{7H}$**Er**, $^{7HMe}$**Dy**, and $^{7HMe}$**Er** exhibit $U_{cal}$ values of 20.4, 251, 23, and 254 cm$^{-1}$, respectively. The axiality is already lost here for the Dy(III) ($g_{xx}$ = 0.0245, $g_{yy}$ = 0.0894 and $g_{zz}$ = 11.3355), stabilizing the lower $m_J$ state as the ground state ($m_J$ = ±9/2). The axiality propped up significantly for Er(III) ion with little or very little transverse anisotropy ($g_{xx}$ = 0.0, $g_{yy}$ = 0.0, $g_{zz}$ = 17.9485). The $g_{zz}$ axis is titled by ∼8.4° with respect to the pseudo-$C_7$ axis for Er(III) ion, and similarly, for Dy(III) ion, the $g_{zz}$ axis started to deviate from the pseudo-$C_7$ axis by ∼67° angle. Although similar di-arene complexes are not reported, mono heptatrienyl arene of Dy(III) and Er(III) analogues are reported ([K-(THF)$_2$Er$_2$($C_7H_7$) (N(SiMe$_3$)$_2$)$_4$][50] where Er(III) analogue is found to be superior compared to Dy(III) affirming our calculated results. For eight-membered systems as well, four molecules are modelled with the $^{8H}$**Dy**, $^{8H}$**Er**, $^{8HMe}$**Dy**, and $^{8HMe}$**Er** exhibiting $U_{cal}$ values of 34, 191, 71, and 255 cm$^{-1}$, respectively. Only marginal enhancement in the $U_{cal}$ values is noted for Er(III), and this suggests that the strong equatorial ligand required for stabilization of $m_J$ = ±15/2 is already reached with a seven-membered ring and increasing the hapticity further brings only moderate changes. The $g_{zz}$ axis for the Er(III) now lies along the pseudo-$C_8$ axis (with a small tilt angle of 4.5°), while the Dy(III) now deviates from this axis by 121°.

**Comparison of $U_{cal}$ Value Across the Lanthanoarenes.** Moving from four to higher member ring, the $U_{cal}$ values decrease gradually in the order $^{4H/HMe}$**Dy** > $^{5H/HMe}$**Dy** > $^{6H/HMe}$**Dy** > $^{7H/Me}$**Dy** ∼ $^{8H/Me}$**Dy**, except $^{5HMe}$**Dy** > $^{4HMe}$**Dy** due to the significant agostic interaction present in $^{4HMe}$**Dy** (see Figure 3a). The increase in ring size increases the size of the π-electron cloud, which interacts with the Dy(III) ion, and leads to the following consequences: (i) they tend to stabilize other excited $m_J$ states, (ii) they reduce the overall CF splitting of the $^6H_{15/2}$ level, (iii) enhance the mixing of the $m_J$ states, (iv) offers significant transverse anisotropy enabling QTM effects, and (v) in the extreme cases of seven- and eight-membered rings, the $m_J$ = |±1/2⟩ ($m_J$ = |±15/2⟩) is stabilized as the ground state. For Er(III) ion, on the other hand, the barrier height diminishes in the reverse order to the Dy(III) as $^{4H/HMe}$**Er** < $^{5H/HMe}$**Er** < $^{6H/HMe}$**Er** < $^{7H/Me}$**Er** ∼ $^{8H/Me}$**Er**, and this is due to an increase in anisotropy along the easy-plane (Figures 2c,d and S2−S4). Switching the metal ion from Dy(III) to Er(III) leads to the exact opposite observation of the above-mentioned points for the prolate Er(III) ion. The larger ring stabilizes the larger $m_J$ level for Er(III) ion, increases the overall CF splitting of the $^4I_{15/2}$ level, and reduces the mixing of excited $m_J$ levels. For this reason, the four, five, and six-membered complexes exhibit SIM characteristics for Dy$^{III}$, while seven- and eight-membered complexes exhibit SIM characteristics for Er$^{III}$ ion.

**Spin Dynamics Using DFT-based Molecular Dynamics Snapshots.** To understand the role of structural distortions in influencing the crystal field parameters and, hence, the effective energy barrier, DFT-based molecular dynamics calculations have been performed on the four- to seven-member ring complexes ($^{4H}$**Dy**/**Er** to $^{7H}$**Dy**/**Er**) for 2000 femtoseconds (fs) (Figures 3b and S9).[63,64] Then ab initio, CASSCF calculations were performed on various snapshots at 200 fs intervals to derive anisotropic parameters. Analysis of various molecular dynamics snapshots primarily reveals three structural distortions: (i) various rotational isomers of the arene ligands such as eclipsed, gauche, and those in between; (ii) various fluxional isomers, where the Ln−C hapticity η alters (along with Ln−C distance); and (iii) alteration of $C_R$−Ln−$C_R$ angle (bending of the arene rings, see Figure 3b for $^{4H}$**Dy**/**Er** and Figure S9 for others in Supporting Information).

Various snapshots in the MD reveal a variation of $C_R$−Ln−$C_R$ angle bending in the range of 133−147° for four-membered arene rings. For five, six, and seven-membered arene complexes, the range is estimated to be 123−148, 155−174, and 156−163°, respectively. This suggests that angle bending is significant for five-membered arene systems (variation of 25°) and least for seven-membered arene complex (7°). It is important to note here that the C−H bond vibrations that are found to be responsible for the reduction of $T_B$ values in dysprosocenium SIMs are correlated to $C_R$−Ln−$C_R$ angle bending. Thus, a larger bending invariably suggests a scenario of reduction in $T_B$ values. Many of the geometrical fluctuations noted here can be correlated to various disorders often noticed in the X-ray structures reported. Ab initio calculations performed on ten snapshot geometries obtained from the MD simulations yield a significant variation in the crystal field parameters, which is also reflected in the estimated $U_{cal}$ values. The analysis of the CF parameters from the above calculations gives an intriguing insight into the geometric distortions observed. Here, the axial CF parameters (example $B_2^0$) are substantially larger than the nonaxial term (example $B_2^1$) parameters for each of the snapshots for $^{4H}$**Dy**. This suggests the perseverance of axial anisotropy and quenching of QTM across all the ensembles (Figures 3c and S5a−c). For $^{4H}$**Er**, a reverse scenario is noted with larger nonaxial parameters, and a stronger QTM at the ground state level leads to the absence of SIM behavior. As the CF parameter varies, the effective energy barrier is also found to vary with $^{4H}$**Dy**, exhibiting the $U_{cal}$ value in the range of 881−1201 cm$^{-1}$ (represented in Figure 3d). This range represents geometries with 8% smaller and 25% larger barrier heights than the minimum energy structure at a temperature of 298 K, a similar variation in the CF parameter is also visible.

The largest variation in the estimated CFP/barrier is observed due to the increase in $C_R$−Dy−$C_R$ angle, and this also alters the associated Dy···H agostic interactions and, hence, the transverse field (2.806 Å vs 3.318 Å, Figure S20). A similar estimate was computed for ten snapshots each for five, six, and seven-membered arene systems [60 snapshots overall considering both Dy(III) and Er(III)]. If we compare the CF parameters of $^{7H}$**Er** and $^{7H}$**Dy** across all snapshots studied, the axial parameters are substantially larger than the nonaxial parameters for the former and vice-versa for the latter. Further,


https://doi.org/10.1021/acs.inorgchem.3c00956
Inorg. Chem. 2023, 62, 9552−9562

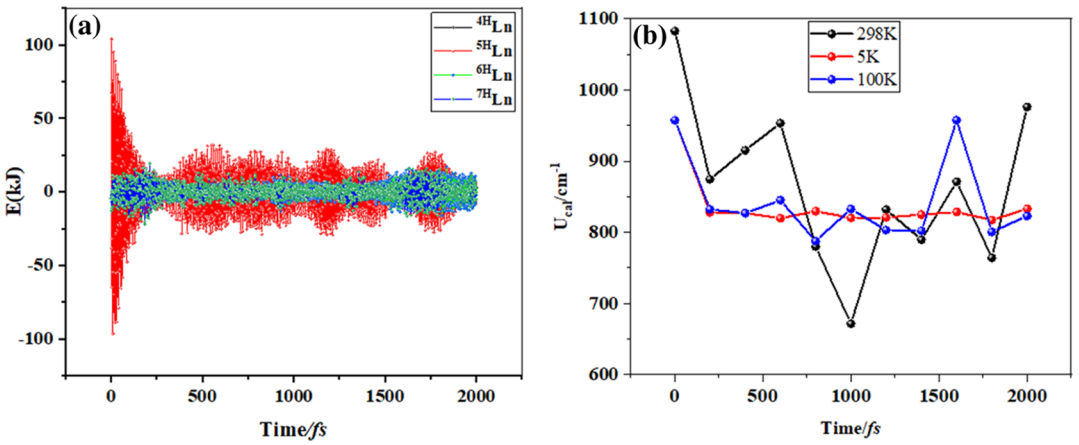


**Figure 4.** (a) Comparison of different fluxional geometry for $^{4H}$**Ln**(black), $^{5H}$**Ln**(red), $^{6H}$**Ln**(green), and $^{7H}$**Ln**(blue) over the 2000 fs. A large deviation in the vibrations for the former has been noticed compared to the later. (b) Variation of $U_{cal}$ value for $^{5H}$**Dy** at different scans and different temperatures.

the variation of the nonaxial parameters, the key to controlling QTM, was found to be minimal for $^{4H}$**Dy**, $^{5H}$**Dy**, $^{6H}$**Dy**, and $^{7H}$**Er** geometries (Figures S5−S7). For all other geometries, the variations in nonaxial parameters across the snapshots are much higher. Further, for Dy(III) five, six, and seven-membered systems, the $U_{cal}$ ranges are 764−954, 478−698, and 24−128 cm$^{-1}$, respectively (Figure 3d). For the five- and six-membered arene complexes of Er(III), the estimated $U_{cal}$ is scattered in the range of ∼10 to 90 cm$^{-1}$ and improved substantially for seven-membered arenes (108−303 cm$^{-1}$).

We have also compared the time evolution of structural distortions with respect to the ring size (Figure 4a) and the substituents (Figure S24). While individually significant variations are noted, if plotted in one energy scale, it is apparent that the $^{4H}$**Ln** exhibit the least fluctuations, and this is perhaps attributed to the stronger and shorter Ln−C distances. The maximal fluctuations are visible for $^{5H}$**Ln** geometries, with a significant decrease in fluctuations/distortions for $^{6H}$**Ln** followed by $^{7H}$**Ln**. As the ring size increases, the angle-bending distortions will likely create significant strain resulting in fewer distortions. Further, if the arene rings are substituted by alkyl groups, the distortions/fluctuations are significantly diminished. While this observation is seemingly correlated to the experimental observation of larger $T_B$ values with bulkier Cp ring, there are likely to be other factors at play as well here. Nevertheless, the $C_R$−Ln−$C_R$ angle bending is found to be one of the important structural distortions that cause variation in the crystal field parameters. This angle bending decreases with (i) an increase in the bulkiness of the Cp ring, (ii) employing a four-membered arene ring as ligand, or (iii) opting for a six- or seven-membered ring system.

To substantiate our discussion further, we have performed temperature-dependent molecular dynamics on complex $^{5H}$**Dy**, which is structurally similar to the reported dysprosocenium complexes exhibiting $T_B$ values in the range of 60−80 K.[2,24] The variable temperature molecular dynamics calculations have been performed by considering a low temperature (5 K), an intermediate temperature (100 K), and room temperature (298 K) for 2000 fs. As the relaxation time for this molecule reaches up to ∼50 s at 77 K, these snapshots resemble the low-energy vibrational geometries whose contributions were found to be determinantal in the relaxation process. Our calculations reveal that at 5 K, there are no significant changes in the crystal field, and the estimated $U_{cal}$ values for various snapshots (ten snapshots) are nearly the same (variation of <±50 cm$^{-1}$, see Figures 4 and S21) except in the 0−200 fs range where a larger reduction is noticed and this is due to a change in $C_R$−Ln−$C_R$ angle from 147 to 135°. For the intermediate temperature at 100 K, these values and CF parameters alter moderately (variation of ±106 cm$^{-1}$). At higher temperatures (298 K), the variation in CF parameters is substantial. However, the shape of the variations is identical to those witnessed at 5 K (red, blue, and black curves in Figure 4b), suggesting the geometrical variations seen at one temperature are magnified at a higher temperature, and no new geometries with substantially different $U_{cal}$ value appear even at 298 K. As we move to higher and higher temperatures, many of the geometries and CF parameters are found to vary drastically. For example, at 298 K, the geometry at 1000 fs yields the lowest $U_{cal}$ value of 671 cm$^{-1}$, while the geometry at 2000 fs yields the largest $U_{cal}$ value (976 cm$^{-1}$). This is essentially due to variation in the Dy···$C_R$ distance (change is ±0.2 Å) and $C_R$−Dy−$C_R$ angle (change is ±11°). These geometric alterations alter the g-anisotropy as well as the 0th, 1st, and 2nd-order CF parameters (Figure S22). As the temperature increases, the structural variations in the snapshots are larger, causing faster relaxation of magnetization. An increase in the population of these distorted geometries, which includes geometries exhibiting extreme fluxionality, tends to reduce the overall blocking temperatures/barriers. In simple terms, if we analyze the CF parameters across the snapshot, a "V" shaped curve suggests a strong presence of SIMs, while a figure-of-eight-type curve suggests loss of SIMs due to structural variation. Thus, these new theoretical tools that were tested on this important set of complexes, offer direct insights into the relationship between the Ln(III) ion and the size of the rings and can be utilized to make robust predictions for other SIMs.

To check the importance of lower energy frequencies in spin relaxation, several CASSCF calculations were performed on asymmetric stretching at $\omega$ = 310 and 230 cm$^{-1}$ for $^{5H}$**Dy** and $^{4H}$**Dy**, respectively, as these vibrations have significant oscillator strength and also match with the KD1-KD2 gap as suggested earlier.[2,20,28] These frequencies were found to be shifted to higher/lower values in different snapshots, suggesting time evolution of the vibrations with respect to various fluxional


https://doi.org/10.1021/acs.inorgchem.3c00956
Inorg. Chem. 2023, 62, 9552−9562

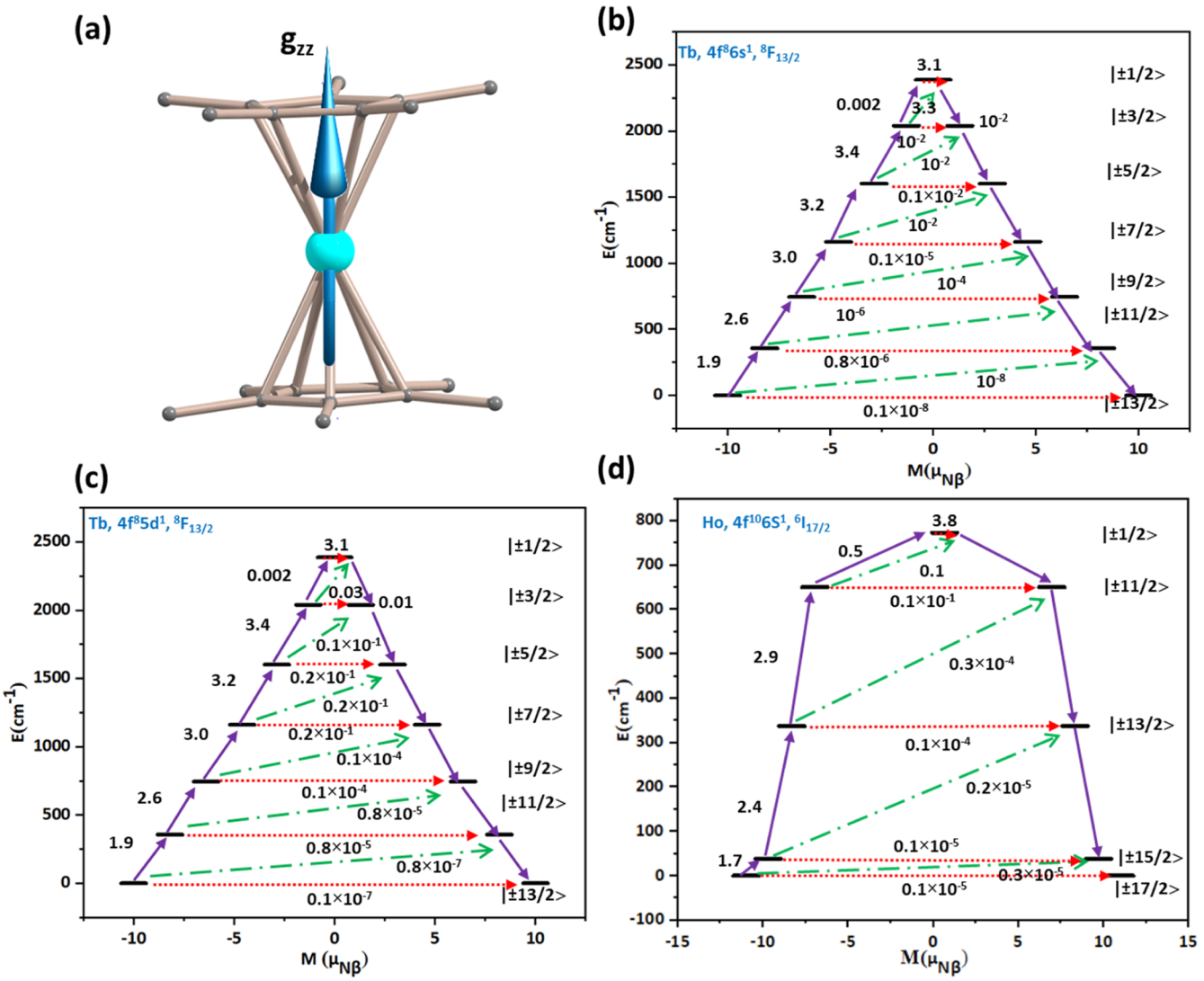


**Figure 5.** (a) Optimized structure of Tb($Cp^{Me5}$)$_2$; light blue arrow shows $g_{zz}$ direction. Color code: cyan—Tb and gray—C. Hydrogen atoms are omitted for clarity. Magnetization blocking diagram of (b) $^{5Me}$**Tb**(II) [$4f^8 5d^0 6s^1$], (c) $^{5Me}$**Tb**(II) [$4f^8 5d^1 6s^0$], and (d) $^{5Me}$**Ho**(II) [$4f^{10} 5d^0 6s^1$].

conformers (see Figures S30 and S31). A total of six displaced geometry were considered here along the vibrational mode with displacement ±0.5, ±1.0, and ±1.5 Å. The mechanism of magnetization relaxation was developed after the analyzing CF parameters (see Figures S7 and S8 and Tables S22 and S23). The CF parameter, $B_k^q$ ($k$ = 2, $q$ = ±2, ±1, 0) of the displaced geometry deviated largely from the optimized geometry. It is found that this asymmetric stretching computed is associated with a large change in $B_2^{\pm 1}$ CF parameter $\left(\left(\frac{\partial B_2^{\pm 1}}{\partial q}\right)^2 > 1000\right)$ and, therefore, should cause the $\left|\frac{15}{2}, \pm\frac{15}{2}\right\rangle \rightarrow \left|\frac{15}{2}, \pm\frac{13}{2}\right\rangle$ transition for magnetization relaxation.[2,28] The asymmetric stretching vibrations computed for $^{5H}$Dy and $^{4H}$Dy cause a decrease in the axial crystal field strength of the ligand and enhance the transverse anisotropy due to the possibility of Dy···H−C agnostic interaction, and, hence, the low energy vibrations contribute to the magnetization relaxation.

**Structure and Magnetization Relaxation of Lanthanoarenes(II).** To understand how the variation in the oxidation state influences the magnetic anisotropy, we have modelled three [Ln($Cp^{Me5}$)$_2$] ($Cp^{Me5}$ = pentamethylcyclopentadienyl) complexes [$^{5Me}$**Dy**(II); $^{5Me}$**Tb**(II) and $^{5Me}$**Ho**(II)] from their reported X-ray structures analogue of [Ln($Cp^{ipr5}$)$_2$].[51] The models were first optimized at DFT levels (G09; B3LYP/6-31G*). After the geometry optimization, geometrical parameters were analyzed, and it has been found that all three $^{5Me}$**Tb**(II), $^{5Me}$**Dy**(II), and $^{5Me}$**Ho**(II) molecules show a $C_R$−Ln−$C_R$ angle of 179.1° that is very close to linearity found in [Ln($Cp^{ipr5}$)$_2$] (see Figure 5a). The Ln−X and Ln−C bond distances were 2.368 and 2.661 Å, respectively.

From magnetic susceptibility and DFT calculations, Long and co-workers suggested a $4f^n 5d^1 6s^0$ configuration with a strong mixing with the $4f^n 5d^0 6s^1$ configuration.[47] While Ungur and co-workers suggest a $4f^n 5d^0 6s^1$ configuration based on calculations performed on diatomic [LnO] species,[65] to perform the CASSCF/RASSI-SO/SINGLE_ANISO calculation of the model complexes, we have chosen three different electronic configurations: (i) $4f^n 5d^1 6s^0$, (ii) $4f^n 5d^0 6s^1$, and (iii) $4f^{n+1} 5d^0 6s^0$. Among these configurations, the $4f^{n+1} 5d^0 6s^0$ is found to be very high in energy for all three metal ions (more than 35,000 cm$^{-1}$) and, therefore, has not been considered further. For configurations (i) and (ii), our calculations reveal


https://doi.org/10.1021/acs.inorgchem.3c00956
Inorg. Chem. 2023, 62, 9552−9562

strong mixing of both configurations, with the $4f^n5d^06s^1$ configuration being lower in energy by only ∼2 $cm^{-1}$ for $^{5Me}$**Tb**(II) compared to the $4f^n5d^16s^0$ configuration. The magnetic anisotropy is found to be strongly Ising in nature ($g_x = g_y = 0.0$ and $g_z = 20.015$) with predominantly $m_J = |\pm 13/2\rangle$ ground state and $g_{zz}$ axis passing through the Cp rings. The principle magnetization axis for the first excited state KDs deviates from the ground state by an angle of 0.001°, and the largest deviation (0.053°) was found at the 6th excited state (see Table S15). Similarly, a very high magnetic anisotropy was found for $^{5Me}$**Dy**(II) and $^{5Me}$**Ho**(II) complex as well (see Tables S16 and S17). As we move from the ground state to the higher excited state, transverse anisotropy is prominent, resulting in the relaxation of magnetization. In the case of $^{5Me}$Tb(II), the magnetization relaxation occurs through the 5th excited state via the Orbach and TA-QTM pathway (see Figure 5b,c), unveiling the $U_{cal}$ value of 2039 $cm^{-1}$. Due to the strong mixing of the states, the computed $U_{cal}$ is similar for both configurations, $4f^n5d^16s^0$ and $4f^n5d^06s^1$. As $^{5Me}$**Dy**(II) is a non-Kramer system, a tunnel splitting $\Delta_t$ of 0.014 $cm^{-1}$ was estimated between $|+6\rangle$ to $|-6\rangle$ corresponding to the 2nd excited state, with complete blocking of magnetization below this level (see Table S14), yielding a $U_{cal}$ value of ∼1260 $cm^{-1}$. For the $^{5Me}$**Ho**(II) compound, the ground state is found to be $m_J = |\pm 17/2\rangle$ exhibiting a strong Ising type anisotropy with $g_x = g_y = 0.0$ and $g_z = 22.007$, the largest $g_z$ value reported thus far. However, a strong transverse anisotropy is noted in the 3rd excited state, causing magnetization relaxation, yielding a barrier height of 773 $cm^{-1}$ for this compound (see Figure 5d).

**Design Clues to Improve the Magnetic Behavior of Lanthanoarenes.** From the detailed DFT, molecular dynamics, and ab initio CASSCF calculations, the following design clues to improve the magnetic properties of lanthanoarenes are revealed: (i) we found that the fluxional behavior of the arene rings induces transverse anisotropy that causes magnetization relaxation and, hence, reduction in the barrier height/blocking temperature. The fluxionality was found to be least for the four-membered ring system and significant for the five-membered ring, but for the six/seven-membered ring systems, it was found to fall in-between. This suggests that a dysprosocenium complex with a four-membered ring would yield the largest barrier height; however, the four-membered arene ring should have the least alkyl substitution to avoid a strong agostic interaction that undercuts the barrier significantly. While this runs counter to the idea of larger alkyl groups that are proposed to increase the axiality and the $C_R$−Ln−$C_R$ angle, considering the significant Dy···H−C agostic interaction detected, smaller substituents are suggested. Alternatively, encapsulating such molecules in SWCNT or MOFs containing significant aromatic groups could further aid in avoiding fluxionality via $\pi$...$\pi$ stacking. (ii) As the fluxional behavior for the seven-membered rings is minimal, the Er(III) molecule with seven-membered rings on both sides could be targeted to achieve this feat; however, the barrier heights for magnetization are relatively small, and electron-donating substituents at the arene ring would help to enhance the barrier height further in this case. (iii) Agostic interactions are found to be an important factor that injects transverse anisotropy in many of the complexes studied, including the four-membered arene systems. Further, the vibrational mode responsible for relaxation was also found to possess agostic interaction at certain displacement values, reiterating the need to avoid this interaction. This interaction can be avoided by (a) destabilizing the empty 5d orbitals of the Ln ions that are involved in this interaction, (b) replacing the C−H bonds with heavier analogues such as C−X (X = halogen), and (c) less electron-deficient metal-ion such as Ln(II) that facilitate weaker/no agostic interactions, suggesting Tb(II) with four-membered rings could be an attractive target. (iii) Further reduction of Ln(III) ion was found to increase the $C_R$−Ln−$C_R$ angle, which is expected to increase the axiality even further. Considering this observation, if such a complex with four-membered arenes is made, this will avoid strong agostic interactions, thanks to the $C_R$−Ln−$C_R$ angle and relatively smaller charge on the Ln ion. The Ln(II) systems are also ideal for easy encapsulation thanks to charge neutrality.[46]

## CONCLUSIONS

In summary, by studying 25 lanthanoarene complexes, having a general formula $[(\eta^p\text{-}C_nR_n)_2Ln]^m$ ($n$ = 4−8), we unravel the relationship between SIMs behavior and the ring size of the arenes. Our study unveils that a smaller ring size (four to six) is suitable for Dy(III) ion, whereas the larger rings (seven and eight) yield better SIM characteristics with Er(III) ion. For the four-member arenes, the $SiMe_3$-substituted molecule effective barrier is found to be 1442 $cm^{-1}$, and this is one of the largest values for such systems and offers hope to fine-tune the ligand further to enhance the axial limit. The detailed bonding analysis performed as per the AIM theory indicates a Ln···H agostic interaction in many of the systems studied. Although electron-donating substituents at the ring position are found to enhance the crystal field splitting and, hence, the anisotropy, in some cases, they also offer a strong Ln···H−C agostic interaction that gives rise to strong equatorial ligation, stabilizing lower $m_J$ states, inducing strong tunneling, and spoiling the SIM characteristics. To probe the spin dynamics of these systems, we have employed DFT-based molecular dynamics followed by CASSCF studies on these snapshots for eight arene complexes. These studies reveal that the number of conformers that are accessible is correlated to the nature of the ring size and the metal ions. Particularly, Dy(III) ion with $n$ = 4−6 showed a "v" shaped behavior if CF parameters were plotted for different molecular dynamics snapshots and exhibited a figure of eight plot when $n$ = 7−8. For Er(III) ion, on the other hand, a reverse scenario is noted, offering a viable tool to find suitable partners between lanthanide and the arene rings.

The molecular dynamics study, coupled with ab initio calculations, reveals various geometric distortions that include fluxionality affecting the crystal field parameters and, hence, the magnetic characteristics. While the dynamics performed at 5 K reveal a rigid geometry with very few distortions and variations in the magnetic characteristics, enhancing the temperature to 100 and 298 K was found to bring various structural fluctuations that cause a reduction in barrier height of magnetization reversal and suggest that enhancing the $T_B$ values in these family of complexes may bring other complexities. On the same energy scale, the least fluctuations are noted for four-membered arenes, followed by seven, six, and five. While this is counterintuitive, the distortions are correlated to the strength of the Ln···C bond, and the larger ring sizes cause significant strain on $C_R$−Ln−$C_R$ bending. Many of these fluctuations are also found to be arrested or minimized upon substitution of alkyl groups at the arene rings or opting for four-membered arenes for an oblate lanthanide ion. The other problems, such as agostic interactions, are


https://doi.org/10.1021/acs.inorgchem.3c00956
Inorg. Chem. 2023, 62, 9552−9562

expected to kick in with smaller arenes. We suggest various design clues, including utilizing Ln(II) ions, to avoid such toxic interactions. These points need to be kept in mind for the futuristic design of arene-based SIMs.

## ■ ASSOCIATED CONTENT

### Supporting Information

The Supporting Information is available free of charge at https://pubs.acs.org/doi/10.1021/acs.inorgchem.3c00956.

This contains additional figures, optimized geometries, tables containing ab initio calculated parameters, molecular dynamics figures, AIM analysis, spin-phonon coupling figures, computed frequencies, orbitals employed for the CAS reference space, and the final optimized coordinates for all the species reported (PDF)

## ■ AUTHOR INFORMATION


### Corresponding Author

**Gopalan Rajaraman** − *Department of Chemistry, IIT Bombay, Mumbai 400076, India;* orcid.org/0000-0001-6133-3026; Email: rajaraman@chem.iitb.ac.in

### Authors

**Abinash Swain** − *Department of Chemistry, IIT Bombay, Mumbai 400076, India*

**Rupesh Kumar Tiwari** − *Department of Chemistry, IIT Bombay, Mumbai 400076, India*

**Munmun Khatua** − *Department of Chemistry, IIT Bombay, Mumbai 400076, India*

Complete contact information is available at: https://pubs.acs.org/10.1021/acs.inorgchem.3c00956


### Author Contributions

†A.S. and R.K.T. contributed equally to this manuscript.

### Notes

The authors declare no competing financial interest.

## ■ ACKNOWLEDGMENTS

We thank SERB (SB/SJF/2019-20/12; CRG/2022/001697) for funding. A.S. and R.K.T. thank UGC/CSIR for the fellowship.

## ■ REFERENCES


(1) Gatteschi, D.; Sessoli, R.; Villain, J. *Molecular Nanomagnets*; Oxford University Press on Demand, 2006; Vol. 5.

(2) Goodwin, C. A.; Ortu, F.; Reta, D.; Chilton, N. F.; Mills, D. P. Molecular magnetic hysteresis at 60 kelvin in dysprosocenium. *Nature* **2017**, *548*, 439−442.

(3) Bogani, L.; Wernsdorfer, W. Molecular spintronics using single-molecule magnets. *Nat. Mater.* **2008**, *7*, 179−186.

(4) Leuenberger, M. N.; Loss, D. Quantum computing in molecular magnets. *Nature* **2001**, *410*, 789−793.

(5) Heras Ojea, M. J.; Maddock, L. C.; Layfield, R. A. Lanthanide organometallics as single-molecule magnets. *Organometallic Magnets*; Springer Nature, 2019, pp 253−280.

(6) Chakraborty, A.; Day, B. M.; Durrant, J. P.; He, M.; Tang, J.; Layfield, R. A. Double Ligand Activation in Silyl-Substituted Rare-Earth Cyclobutadienyl Complexes. *Organometallics* **2019**, *39*, 8−12.

(7) Zhu, Z.; Guo, M.; Li, X.-L.; Tang, J. Molecular magnetism of lanthanide: Advances and perspectives. *Coord. Chem. Rev.* **2019**, *378*, 350−364.

(8) Gatteschi, D.; Sessoli, R. Quantum tunneling of magnetization and related phenomena in molecular materials. *Angew. Chem., Int. Ed.* **2003**, *42*, 268−297.

(9) Latendresse, T. P.; Bhuvanesh, N. S.; Nippe, M. Hard single-molecule magnet behavior by a linear trinuclear lanthanide−[1] metallocenophane complex. *J. Am. Chem. Soc.* **2017**, *139*, 14877−14880.

(10) Singh, S. K.; Gupta, T.; Rajaraman, G. Magnetic anisotropy and mechanism of magnetic relaxation in Er(III) single-ion magnets. *Inorg. Chem.* **2014**, *53*, 10835−10845.

(11) Swain, A.; Sharma, T.; Rajaraman, G. Strategies to quench quantum tunneling of magnetization in lanthanide single molecule magnets. *Chem. Commun.* **2023**, *59*, 3206−3228.

(12) Liu, J.-L.; Chen, Y.-C.; Tong, M.-L. Symmetry strategies for high performance lanthanide-based single-molecule magnets. *Chem. Soc. Rev.* **2018**, *47*, 2431−2453.

(13) Rinehart, J. D.; Long, J. R. Exploiting single-ion anisotropy in the design of f-element single-molecule magnets. *Chem. Sci.* **2011**, *2*, 2078−2085.

(14) Ungur, L.; Le Roy, J. J.; Korobkov, I.; Murugesu, M.; Chibotaru, L. F. Fine-tuning the local symmetry to attain record blocking temperature and magnetic remanence in a single-ion magnet. *Angew. Chem.* **2014**, *126*, 4502−4506.

(15) Meihaus, K. R.; Long, J. R. Magnetic blocking at 10 K and a dipolar-mediated avalanche in salts of the bis ($\eta^8$-cyclooctatetraenide) complex $[Er(COT)2]^-$. *J. Am. Chem. Soc.* **2013**, *135*, 17952−17957.

(16) Bühl, M.; Grigoleit, S. Molecular dynamics of neutral and protonated ferrocene. *Organometallics* **2005**, *24*, 1516−1527.

(17) Chibotaru, L. F.; Ungur, L. Ab initio calculation of anisotropic magnetic properties of complexes. I. Unique definition of pseudospin Hamiltonians and their derivation. *J. Chem. Phys.* **2012**, *137*, 064112.

(18) Kohn, W.; Becke, A. D.; Parr, R. G. Density functional theory of electronic structure. *J. Phys. Chem.* **1996**, *100*, 12974−12980.

(19) Fritsch, D.; Koepernik, K.; Richter, M.; Eschrig, H. Transition metal dimers as potential molecular magnets: A challenge to computational chemistry. *J. Comput. Chem.* **2008**, *29*, 2210−2219.

(20) Singh, M. K.; Yadav, N.; Rajaraman, G. Record high magnetic exchange and magnetization blockade in $Ln_2@C_{79}N$ (Ln= Gd(III) and Dy(III)) molecules: a theoretical perspective. *Chem. Commun.* **2015**, *51*, 17732−17735.

(21) Liu, F.; Krylov, D. S.; Spree, L.; Avdoshenko, S. M.; Samoylova, N. A.; Rosenkranz, M.; Kostanyan, A.; Greber, T.; Wolter, A. U.; Büchner, B.; et al. Single molecule magnet with an unpaired electron trapped between two lanthanide ions inside a fullerene. *Nat. Commun.* **2017**, *8*, 16098.

(22) Reta, D.; Kragskow, J. G.; Chilton, N. F. Ab initio prediction of high-temperature magnetic relaxation rates in single-molecule magnets. *J. Am. Chem. Soc.* **2021**, *143*, 5943−5950.

(23) Rosaleny, L. E.; Zinovjev, K.; Tuñón, I.; Gaita-Ariño, A. A first peek into sub-picosecond dynamics of spin energy levels in magnetic biomolecules. *Phys. Chem. Chem. Phys.* **2019**, *21*, 10908−10913.

(24) Lunghi, A.; Totti, F.; Sanvito, S.; Sessoli, R. Intra-molecular origin of the spin-phonon coupling in slow-relaxing molecular magnets. *Chem. Sci.* **2017**, *8*, 6051−6059.

(25) Albino, A.; Benci, S.; Atzori, M.; Chelazzi, L.; Ciattini, S.; Taschin, A.; Bartolini, P.; Lunghi, A.; Righini, R.; Torre, R.; Totti, F.; Sessoli, R. Temperature dependence of spin−phonon coupling in [VO (acac) 2]: A computational and spectroscopic study. *J. Phys. Chem. C* **2021**, *125*, 22100−22110.

(26) Briganti, M.; Santanni, F.; Tesi, L.; Totti, F.; Sessoli, R.; Lunghi, A. A complete ab initio view of Orbach and Raman spin−lattice relaxation in a dysprosium coordination compound. *J. Am. Chem. Soc.* **2021**, *143*, 13633−13645.

(27) Ullah, A.; Cerdá, J.; Baldoví, J. J.; Varganov, S. A.; Aragó, J.; Gaita-Arino, A. In silico molecular engineering of dysprosocenium-based complexes to decouple spin energy levels from molecular vibrations. *J. Phys. Chem. Lett.* **2019**, *10*, 7678−7683.

(28) Day, B. M.; Guo, F.-S.; Layfield, R. A. Cyclopentadienyl ligands in lanthanide single-molecule magnets: One ring to rule them all? *Acc. Chem. Res.* **2018**, *51*, 1880−1889.

(29) Harriman, K. L.; Le Roy, J. J.; Ungur, L.; Holmberg, R. J.; Korobkov, I.; Murugesu, M. Cycloheptatrienyl trianion: an elusive

bridge in the search of exchange coupled dinuclear organolanthanide single-molecule magnets. *Chem. Sci.* **2017**, *8*, 231−240.
(30) Guo, F.-S.; Day, B. M.; Chen, Y.-C.; Tong, M.-L.; Mansikkamäki, A.; Layfield, R. A. Magnetic hysteresis up to 80 kelvin in a dysprosium metallocene single-molecule magnet. *Science* **2018**, *362*, 1400−1403.
(31) Frisch, M.; Trucks, G.; Schlegel, H.; Scuseria, G.; Robb, M.; Cheeseman, J.; Scalmani, G.; Barone, V.; Mennucci, B.; Petersson, G. *Gaussian 09*. Revision A.01; Gaussian Inc.: Wallingford CT, 2009; p 139.
(32) Frisch, A. *Gaussian 09W Reference*; Gaussian Inc.: Wallingford, USA, 2009; p 25.
(33) Feller, D. The role of databases in support of computational chemistry calculations. *J. Comput. Chem.* **1996**, *17*, 1571−1586.
(34) De Oliveira, A.; Ferreira, I.; Campos, C.; Jorge, F.; Fantin, P. Segmented all-electron basis sets of triple zeta quality for the lanthanides: application to structure calculations of lanthanide monoxides. *J. Mol. Model.* **2019**, *25*, 38−39.
(35) Rassolov, V. A.; Pople, J. A.; Ratner, M. A.; Windus, T. L. 6-31G* basis set for atoms K through Zn. *J. Chem. Phys.* **1998**, *109*, 1223−1229.
(36) Lee, C.; Yang, W.; Parr, R. G. Development of the Colle-Salvetti correlation-energy formula into a functional of the electron density. *Phys. Rev. B: Condens. Matter Mater. Phys.* **1988**, *37*, 785−789.
(37) Becke, A. D. Density-functional exchange-energy approximation with correct asymptotic behavior. *Phys. Rev. A: At., Mol., Opt. Phys.* **1988**, *38*, 3098−3100.
(38) Bader, R. F. Atoms in molecules. *Acc. Chem. Res.* **1985**, *18*, 9−15.
(39) Hutter, J.; Iannuzzi, M.; Schiffmann, F.; VandeVondele, J. cp2k: atomistic simulations of condensed matter systems. *Wiley Interdiscip. Rev.: Comput. Mol. Sci.* **2014**, *4*, 15−25.
(40) Fraternali, F. Restrained and unrestrained molecular dynamics simulations in the NVT ensemble of alamethicin. *Biopolymers* **1990**, *30*, 1083−1099.
(41) Hammer, B.; Hansen, L. B.; Nørskov, J. K. Improved adsorption energetics within density-functional theory using revised Perdew-Burke-Ernzerhof functionals. *Phys. Rev. B: Condens. Matter Mater. Phys.* **1999**, *59*, 7413−7421.
(42) Lunghi, A.; Totti, F.; Sessoli, R.; Sanvito, S. The role of anharmonic phonons in under-barrier spin relaxation of single molecule magnets. *Nat. Commun.* **2017**, *8*, 14620.
(43) Aquilante, F.; Autschbach, J.; Carlson, R. K.; Chibotaru, L. F.; Delcey, M. G.; De Vico, L.; FdezGalván, I.; Ferré, N.; Frutos, L. M.; Gagliardi, L. *Molcas 8: New Capabilities for Multiconfigurational Quantum Chemical Calculations across the Periodic Table*; Wiley Online Library, 2016.
(44) Malmqvist, P.-Å.; Roos, B. O. The CASSCF state interaction method. *Chem. Phys. Lett.* **1989**, *155*, 189−194.
(45) Bolvin, H. An alternative approach to the g-matrix: Theory and applications. *ChemPhysChem* **2006**, *7*, 1575−1589.
(46) Lawley, K. P. *Ab Initio Methods in Quantum Chemistry, Volume 69, Part 2*; John Wiley & Sons, 2009.
(47) Widmark, P.-O.; Zobel, J. P.; Vysotskiy, V. P.; Tsuchiya, T.; Veryazov, V. New compact density matrix averaged ANO basis sets for relativistic calculations. *J. Chem. Phys.* **2018**, *149*, 194102.
(48) Roos, B. O.; Lindh, R.; Malmqvist, P.-Å.; Veryazov, V.; Widmark, P.-O.; Borin, A. C. New relativistic atomic natural orbital basis sets for lanthanide atoms with applications to the Ce diatom and LuF3. *J. Phys. Chem. A* **2008**, *112*, 11431−11435.
(49) Roos, B. O.; Lindh, R.; Malmqvist, P.-Å.; Veryazov, V.; Widmark, P.-O. New relativistic ANO basis sets for transition metal atoms. *J. Phys. Chem. A* **2005**, *109*, 6575−6579.
(50) Nabi, R.; Tiwari, R. K.; Rajaraman, G. In silico strategy to boost stability, axiality, and barrier heights in dysprocenium SIMs via SWCNT encapsulation. *Chem. Commun.* **2021**, *57*, 11350−11353.
(51) Gould, C. A.; McClain, K. R.; Yu, J. M.; Groshens, T. J.; Furche, F.; Harvey, B. G.; Long, J. R. Synthesis and magnetism of neutral, linear metallocene complexes of terbium (II) and dysprosium (II). *J. Am. Chem. Soc.* **2019**, *141*, 12967−12973.
(52) Sharma, T.; Singh, M. K.; Gupta, R.; Khatua, M.; Rajaraman, G. In silico design to enhance the barrier height for magnetization reversal in Dy (iii) sandwich complexes by stitching them under the umbrella of corannulene. *Chem. Sci.* **2021**, *12*, 11506−11514.
(53) Harriman, K. L.; Murugesu, M. An organolanthanide building block approach to single-molecule magnets. *Acc. Chem. Res.* **2016**, *49*, 1158−1167.
(54) Dey, S.; Velmurugan, G.; Rajaraman, G. How important is the coordinating atom in controlling magnetic anisotropy in uranium (iii) single-ion magnets? A theoretical perspective. *Dalton Trans.* **2019**, *48*, 8976−8988.
(55) Duan, C.-K.; Tanner, P. A. What use are crystal field parameters? A chemist's viewpoint. *J. Phys. Chem. A* **2010**, *114*, 6055−6062.
(56) Walter, U. Treating crystal field parameters in lower than cubic symmetries. *J. Phys. Chem. Solids* **1984**, *45*, 401−408.
(57) Ungur, L.; Chibotaru, L. F. Strategies toward high-temperature lanthanide-based single-molecule magnets. *Inorg. Chem.* **2016**, *55*, 10043−10056.
(58) Ungur, L.; Thewissen, M.; Costes, J.-P.; Wernsdorfer, W.; Chibotaru, L. F. Interplay of strongly anisotropic metal ions in magnetic blocking of complexes. *Inorg. Chem.* **2013**, *52*, 6328−6337.
(59) Goodwin, C. A.; Reta, D.; Ortu, F.; Chilton, N. F.; Mills, D. P. Synthesis and electronic structures of heavy lanthanide metallocenium cations. *J. Am. Chem. Soc.* **2017**, *139*, 18714−18724.
(60) King, W. A.; Di Bella, S.; Lanza, G.; Khan, K.; Duncalf, D. J.; Cloke, F. G. N.; Fragala, I. L.; Marks, T. J. Metal− Ligand Bonding and Bonding Energetics in Zerovalent Lanthanide, Group 3, Group 4, and Group 6 Bis (arene) Sandwich Complexes. A Combined Solution Thermochemical and ab Initio Quantum Chemical Investigation. *J. Am. Chem. Soc.* **1996**, *118*, 627−635.
(61) King, W. A.; Marks, T. J.; Anderson, D. M.; Duncalf, D. J.; Cloke, F. G. N. Organo-f-element bonding energetics. Large magnitudes of metal arene bond enthalpies in zero-valent lanthanide sandwich complexes. *J. Am. Chem. Soc.* **1992**, *114*, 9221−9223.
(62) Brennan, J. G.; Cloke, F. G. N.; Sameh, A. A.; Zalkin, A. Synthesis of bis($\eta$-1,3,5-tri-t-butylbenzene) sandwich complexes of yttrium(0) and gadolinium(0); the X-ray crystal structure of the first authentic lanthanide(0) complex,[Gd($\eta$-$Bu^t_3C_6H_3)_2$]. *J. Chem. Soc., Chem. Commun.* **1987**, *21*, 1668−1669.
(63) Lunghi, A.; Iannuzzi, M.; Sessoli, R.; Totti, F. Single molecule magnets grafted on gold: magnetic properties from ab initio molecular dynamics. *J. Mater. Chem. C* **2015**, *3*, 7294−7304.
(64) Dubrovin, V.; Avdoshenko, S. M. Conformational preferences of endohedral metallofullerenes on Ag, Au, and MgO surfaces: Theoretical studies. *J. Comput. Chem.* **2022**, *43*, 1614−1620.
(65) Zhang, W.; Muhtadi, A.; Iwahara, N.; Ungur, L.; Chibotaru, L. F. Magnetic anisotropy in divalent lanthanide compounds. *Angew. Chem., Int. Ed.* **2020**, *59*, 12720−12724.


https://doi.org/10.1021/acs.inorgchem.3c00956
*Inorg. Chem.* 2023, 62, 9552−9562